Along-Strike Variation of Seismicity Near the Extinct Mid-Ocean Ridge Subducted Beneath the Manila Trench

Gaohua Zhu[1,2,3], Hongfeng Yang[*3,4], Ting Yang[5], and Guangxu Zhang[1,2]

Abstract

The change in seismic activity is explored using data recorded by ocean-bottom seismometers (OBSs) and permanent seismic stations near the extinct Mid-Ocean ridge of the South China Sea (SCS) and the Manila trench. We apply the machine learning–based algorithm EQTransformer to the OBS dataset for seismic event detection and phase picking and then evaluate the precision and compare the time residuals between automatic and manual picks. We derive a catalog of earthquakes in the region and find bending-fault earthquakes in the outer rise at the northern of the Huangyan (Scarborough) Seamount chain, where no historical seismicity was reported in the routine catalog. Abundant outer-rise earthquakes occurred on both sides of the Huangyan (Scarborough) Seamounts chain, but the focal depths vary along the trench. The Wadati–Benioff zone of the eastward subducted SCS oceanic lithosphere can be clearly identified. The focal depths are down to ∼100 km near Luzon island at ∼16° N but deepen southward to a depth of ∼180 km at ∼14° N. Dips of the slab also steepen from north to south, indicating along-strike changes in the geometry of the Manila megathrust.

Cite this article as Zhu, G., H. Yang, T. Yang, and G. Zhang (2022). Along-Strike Variation of Seismicity Near the Extinct Mid-Ocean Ridge Subducted Beneath the Manila Trench, *Seismol. Res. Lett.* **XX**, 1–13, doi: 10.1785/0220220304.

Introduction

Bending faults may occur in the outer rise of subduction zones when bending stresses exceed the yield strength of the incoming plate (Masson, 1991). They are common near a trench and can generate a number of bending-related earthquakes that occur within the outer-rise regions (Craig *et al.*, 2014). Outer-rise earthquakes have become notable for many subduction zones because they can host intraplate earthquakes of great magnitudes, possibly inducing devastating tsunamis (Lay *et al.*, 2010, 2011). Besides, deep outer-rise earthquakes have been regarded as an indicator of large water input via subduction zones, such as outer-rise events occurring at depths of ∼35 km below the seafloor with normal-faulting focal mechanisms in central Mariana (Eimer *et al.*, 2020) and a cluster of outer-rise events deeper than 50 km at southern Mariana (Chen *et al.*, 2022). Therefore, understanding the distribution of the outer-rise seismicity and characterizing the nature of the outer rise of an active trench have become fundamental and necessary.

Although the outer-rise seismicity is an important feature in the trench-outer-rise system, there is little attention to the outer-rise earthquakes of the oceanic lithosphere of the South China Sea (SCS) in response to the loading along the Manila trench, partly due to the lack of near-field observational data. The Manila trench is the eastern boundary of the SCS (Fig. 1) and may be capable of generating megathrust earthquakes and devastating tsunamis (Yu *et al.*, 2018; Li *et al.*, 2022). According to the U.S. Geological Survey (USGS) catalog, interface and slab earthquakes are abundant. In contrast, the outer-rise earthquakes with magnitudes >3.6 are only recorded in the south of Huangyan (Scarborough) Seamount chain, but very few outer-rise earthquakes are reported in the north area of the seamount chain (Fig. 2). Outer-rise earthquakes occur on bending-related faults; therefore, such variations of outer-rise seismicity may indicate heterogeneous bending-related faults and strong variation in stresses of the subducting plate.

Both 2D (Zhang, Lin, *et al.*, 2018) and 3D (Zhang, Sun, *et al.*, 2018) numerical simulations of flexural bending have suggested variable elastic plate thickness along the trench. At the northernmost Manila, the elastic plate thickness of the crust is greater than that of the oceanic crust in south and central Manila because of the subduction zone transferred into the

1. CAS Key Laboratory of Marine Geology and Environment, Center for Ocean Mega-Science, Institute of Oceanology, Chinese Academy of Sciences, Qingdao, China, https://orcid.org/0000-0003-4186-7375 (GaZ); 2. Laboratory for Marine Geology, Qingdao National Laboratory for Marine Science and Technology, Qingdao, China; 3. Earth and Environmental Sciences Programme, Faculty of Science, The Chinese University of Hong Kong, Shatin, Hong Kong, China, https://orcid.org/0000-0002-5925-6487 (HY); 4. Shenzhen Research Institute, The Chinese University of Hong Kong, Shenzhen, China; 5. OBS Laboratory, Department of Ocean Science and Engineering, Southern University of Science and Technology, Shenzhen, China, https://orcid.org/0000-0002-3433-0898 (TY)

*Corresponding author: hyang@cuhk.edu.hk

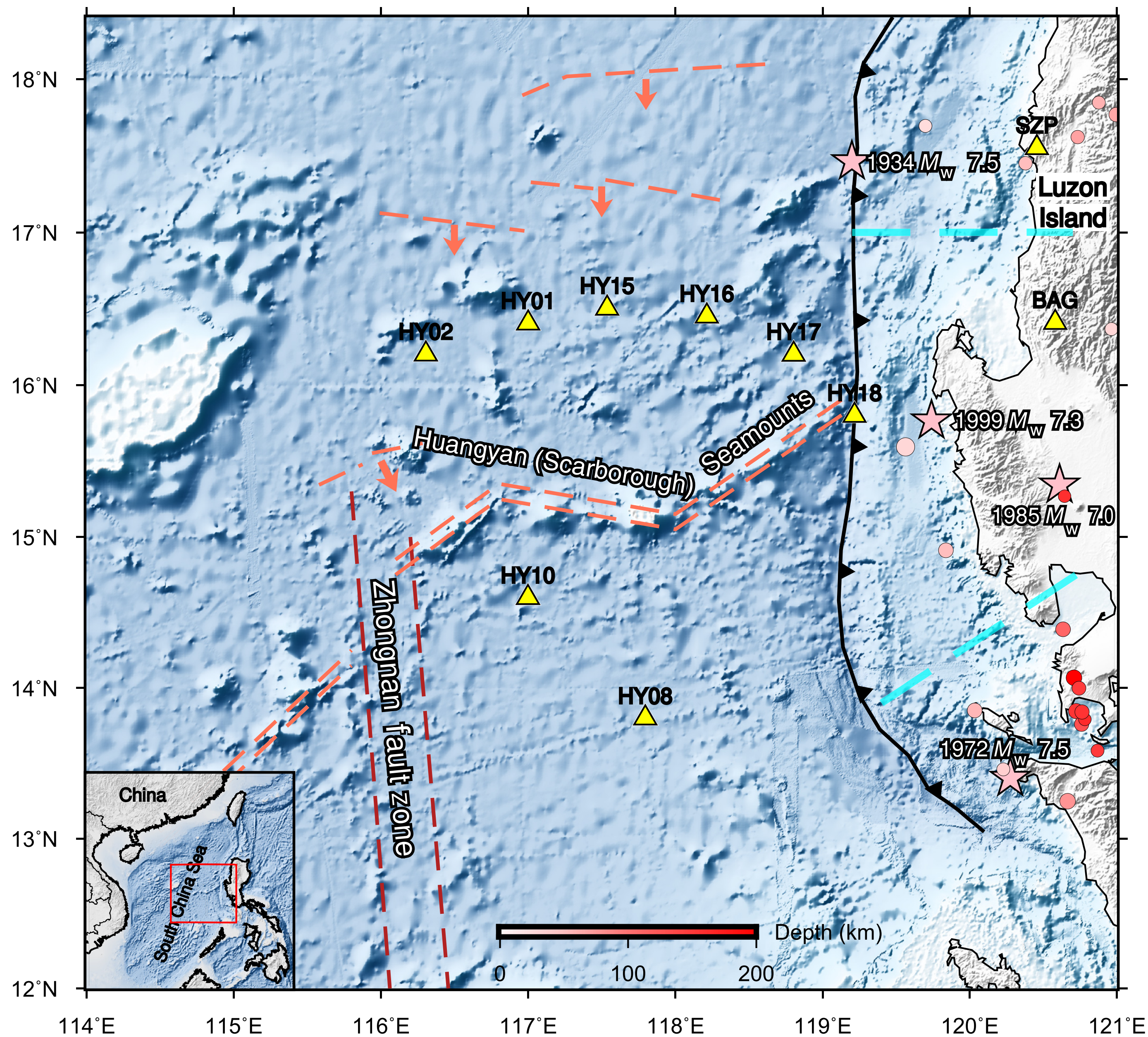

Figure 1. Tectonic settings of South China Sea (SCS) and the Manila trench. The trajectory of extinct fossil ridges (coral dashed lines) is from Guan *et al.* (2021), who established a high-resolution magnetic isochron pattern based on updated magnetic data in the region. The dashed coral lines mark the positions of the extinct Mid-Ocean ridge (MOR) with arrows marking the directions of the ridge jumps. The double dashed coral lines are the final MOR. Two dark red dashed lines trace the Zhongnan fault zone (Li *et al.*, 2014; Zhao *et al.*, 2018). The thick cyan dashed lines mark potential slab tears based on Bautista *et al.* (2001) and Fan *et al.* (2014). The yellow triangles represent the passive-source ocean-bottom seismometer (OBS) array deployed during 2012. The colored dots show 20 earthquakes reported by the U.S. Geological Survey (USGS) catalog during the OBS deployment period. Inset shows location of the study area (red frame). The color version of this figure is available only in the electronic edition.

Taiwan collision zone (Zhang, Lin, *et al.*, 2018; Zhang, Sun, *et al.*, 2018; Zhang *et al.*, 2022). On either side of Huangyan (Scarborough) Seamount chain in central Manila, however, the best-fitting bending parameters from numerical simulations are similar or slightly different, for example, elastic plate thickness of 16 and 15 km, vertical loading of 0.2 and 0.3 10^{12} $\mathrm{N \cdot m^{-1}}$ south and north of the Huangyan (Scarborough) Seamount chain (Zhang, Lin, *et al.*, 2018). The changeless simulation results across the chain seem inconsistent with the heterogeneous historical outer-rise seismicity. One possible reason is that outer-rise earthquakes could have been missed in the historical catalogs because of a lack of detection using near seismic networks.

Improved near-field seismic observation allows us to explore the seismicity pattern near the extinct Mid-Ocean ridge (MOR)

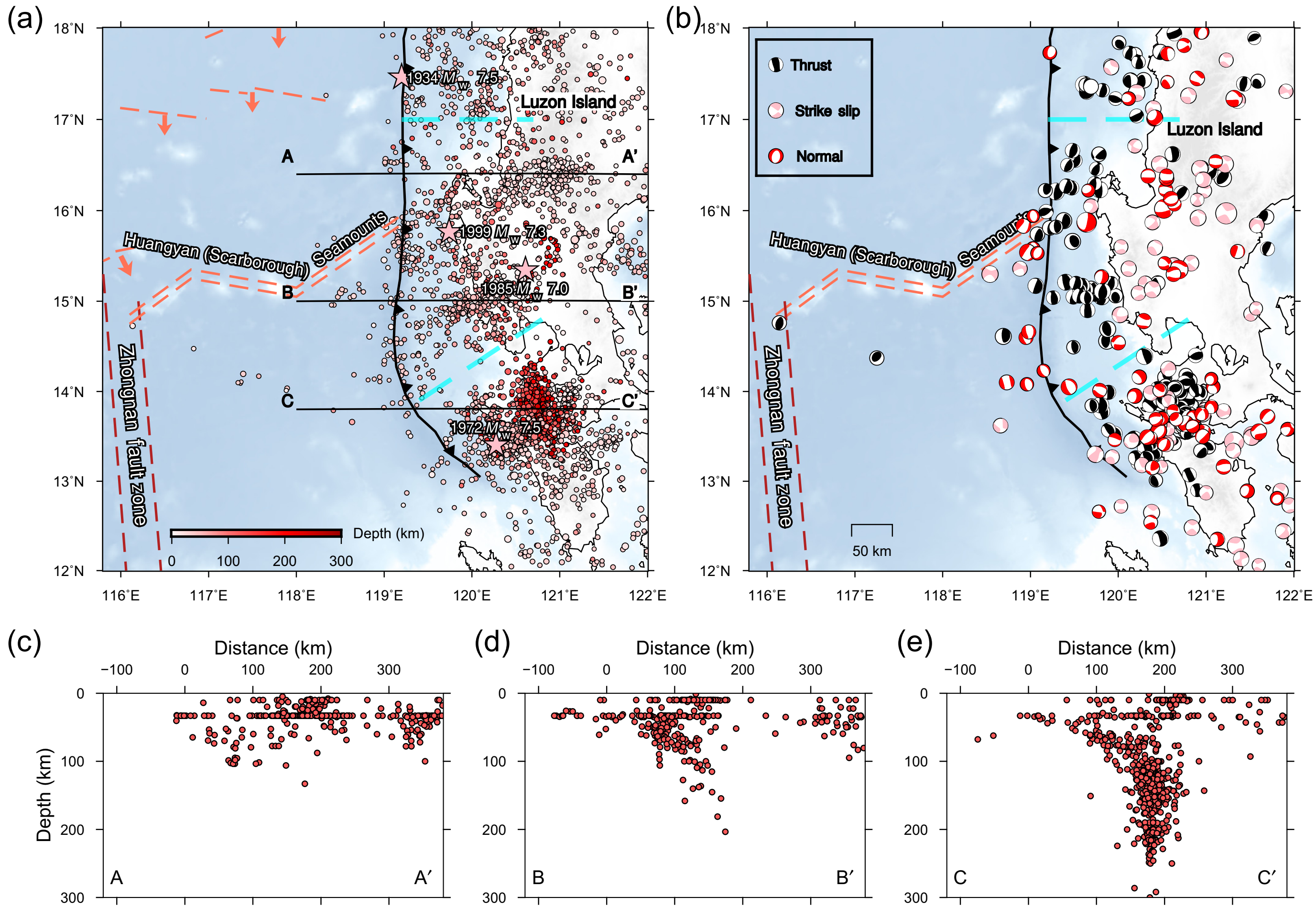

Figure 2. Map of (a) the historical earthquakes from the USGS catalog during 1918–2021 and (b) the focal mechanisms from the Global Centroid Moment Tensor project data catalog. (c–e) The three black lines mark the locations of profiles. The other captions are the same as in Figure 1. The color version of this figure is available only in the electronic edition.

subducted beneath the Manila trench. In this study, we build a catalog of local earthquakes using an ocean-bottom seismometer (OBS) array and adjacent land stations to improve constraints on the outer-rise seismicity and subducted slab in the SCS near the Manila subduction zone. We then examine what outer-rise seismicity can tell us about the deformation of the plate and depict the geometry of subducted slab by examining the cross sections of seismicity near the Manila trench and analyze the seismic activity for any indications of fragmentation of the subducted plate.

Tectonic Setting and Dataset

The oceanic lithosphere of the SCS is eastward subducted beneath the Manila trench. The SCS basin is the largest marginal basin in the northwest Pacific and is formed associated with several continental rifting and seafloor spreading (Briais *et al.*, 1993; He *et al.*, 2001; Chang *et al.*, 2013; Li *et al.*, 2014; Zhao *et al.*, 2018). The seafloor spreading of the SCS oceanic basin is generally believed to start at ~32 Ma and probably ceases at ~16 Ma, during which multiple possible ridge jumps are discovered (Briais *et al.*, 1993; Li *et al.*, 2014; Guan *et al.*, 2021). The axis of the final spreading center of the SCS is presented by the northeast–southwest-trending submarine Huangyan (Scarborough) Seamount chain (Fig. 1), which is suggested to be formed by magmas after the cessation of the seafloor spreading (after ~16 Ma) (Chang *et al.*, 2013). The Zhongnan fault zone is a major boundary for sub-basins within the SCS and is also characterized as a major boundary in magnetic anomalies (Li *et al.*, 2008), but it is seismically less active.

The Manila trench rarely hosts earthquakes greater than a magnitude of 8. The maximum earthquake magnitude recorded in the Manila trench area has been M_w 7.8 since 1560 (Yu *et al.*, 2018). Four earthquakes larger than magnitude 7 have been recorded since 1934 (Figs. 1, 2a). The lack of great megathrust earthquakes is possibly related to the fault geometry heterogeneity caused by along-strike transitions in slab curvature (Yu *et al.*, 2018). To the east of the Manila trench, Luzon island is characterized by a complex deformation pattern as shown by the diverse pattern of focal mechanism solutions (Fig. 2b).

The data were collected from the passive-source OBS array (Liu *et al.*, 2014, 2020) in the SCS basin from April 2012 to December 2012 (Fig. 1). The OBS experiment recovered 11 stations near the extinct MOR and Huangyan (Scarborough) Seamount chain, among which six OBSs had data for 7–8 months and two OBSs only recorded data during the first months due to various issues with the instrumentation. The others did not record any data because of the failure of their data logger. The timing of the OBS had been corrected using the time symmetric analysis based on ambient noise cross correlation (Le *et al.*, 2018). Using the data set, Liu *et al.* (2020) investigated crustal thickness using the receiver function method, which showed the thickest oceanic crust near the Huangyan (Scarborough) Seamount chain. However, Hung *et al.* (2021) got different results using receiver functions that the oceanic crust abruptly thinned at sites close to the seamount chain. In addition to OBS data, we also collected data from two stations sitting on the Luzon island close to the Manila trench.

Detecting Phases by Machine Learning Algorithms

We then employed the machine learning (ML)–based algorithms, PhaseNet (Zhu and Beroza, 2019) and EQTransformer (Mousavi *et al.*, 2020), on the OBS array for earthquake phase detection. These two widely used ML models creatively convert the phase picking into phase probability distributions based on a convolutional neural network. The three-component waveform was 1 Hz high-pass filtered. Seismograms with a sampling rate of 100 Hz and 30 s time segments, with 50% overlap between consecutive segments, were provided as the input. For the EQTransformer, a threshold of 0.1 for *P* and *S* phases was typically used for land stations. Whereas a higher threshold got fewer detections, a lower threshold gave more detections but could damage precision. In the study, considering lower signal-to-noise ratios (SNRs) of OBS data compared with land-station data, we tested thresholds lower than 0.1 (e.g., 0.04, 0.06, and 0.08). To balance the aims of getting more phases and avoiding false detections, we finally retained picks above the probability threshold of 0.06 for *P* and *S* phases. For the PhaseNet, *P*- and *S*-wave arrivals were predicted by PhaseNet with probability thresholds of 0.3.

In total, 161,375 *P*- and 88,571 *S*-wave arrivals were predicted by PhaseNet, and 9244 *P*- and 10,961 *S*-wave arrivals were predicted by EQTransformer. The daily number of predicted phases on each station is shown in Figure 3. For PhaseNet, picks of several stations abruptly increased during the days with air gun sources released (Fig. 3). Unfortunately, the probability of air gun impulses predicted by PhaseNet is higher than the threshold of 0.3, resulting in a large number of false positives of the air gun signals (Fig. 4). In comparison, the daily number of predicted phases by EQTransformer reduces several to tens of times, but the EQTransformer is less affected by the air gun signals (Fig. 3).

Well-trained ML-based automatic phase pickers have been widely used on land-based seismic stations, which show high accuracy for picking *P* and *S* waves on various instruments, including a short period and broadband, high gain and low gain accelerometer and seismometer (e.g., Park *et al.*, 2020; Tan *et al.*, 2021; Wong *et al.*, 2021; Zhou *et al.*, 2021; Jiang *et al.*, 2022; Zhu *et al.*, 2022) and OBS data (Chen *et al.*, 2022; Gong *et al.*, 2022). However, their application of identifying seismic phases from OBS data is quite limited, so the performance of the OBS dataset is not clear. Therefore, we examined the precision of the two algorithms in processing OBS data. Because of lacking predetermined events data with manual labeled *P*- and *S*-wave arrivals in this region, deriving the recall rate is impossible for this study. Instead, only precision was introduced to evaluate the performance. On days without air guns, we randomly chose 100 predicted picks from each algorithm and manually inspected the detections. We repeated the process three times and took the average value as the precision. The precision is defined as $P = T_P/T_P + F_P$, in which T_P, F_P are the number of true and false positives, respectively. Generally, the precision of the EQTransformer is higher than PhaseNet on the OBS stations (Table 1), but both are lower than the precision of land stations.

To assess the uncertainty of the automatic picker, we compared their predicted phases with manually labeled *P*- and *S*-wave arrivals (Fig. 5). We manually picked *P* and *S* phases for the relocated events from the catalog in the later section as the benchmarks and compared these picks with the EQTransformer automatic picks. Figure 5 shows the distribution of time residuals between the automated and human-labeled *P* and *S* picks. The residual distributions of both *P* and *S* phase picks are distinctly narrow and have no obvious biases. The average residuals are −0.07 s and 0.25 s for *P* and *S* waves with a standard deviation of 1.33 s and 2.83 s, respectively. The standard deviation of residuals is about one order of magnitude larger than the travel-time residuals from land stations (Zhou *et al.*, 2021).

Phase Association and Location of Earthquakes

Although the PhaseNet predicted many more potential picks than EQTransformer, the false positives predicted by EQTransformer are much fewer than PhaseNet according to our visual inspection. The larger number of predicted false positives by PhaseNet would disturb the association results, leading to false associations of events. Therefore, we adopted *P*- and *S*-phase arrivals by EQTransformer in the following association and relocation of events.

In total, EQTransformer yielded 9244 *P* and 10,961 *S* picks on the SCS OBS dataset. We associated the phase picks with individual events using the Rapid Earthquake Association and Location package (Zhang *et al.*, 2019). Only events with at least five phases, including at least 1 *P* phase and 1 *S* phase, were retained. The events were preliminarily located at the grid

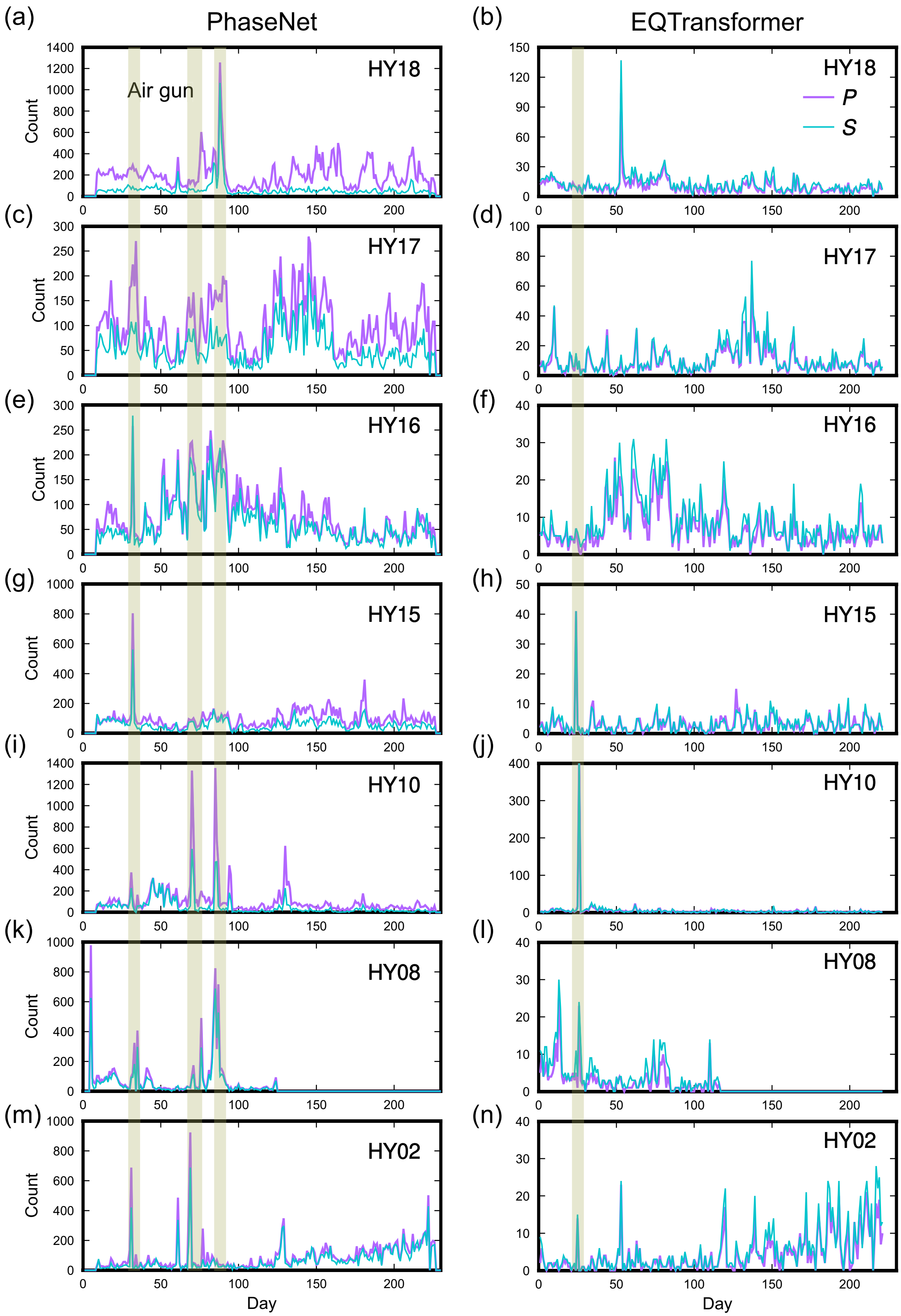

Figure 3. The daily number of predicted *P* and *S* phases on each station by (a,c,e,g,i,k,m) PhaseNet and (b,d,f,h,j,l,n) EQTransformer. The vertical light green bars mark the days with air guns released. The color version of this figure is available only in the electronic edition.

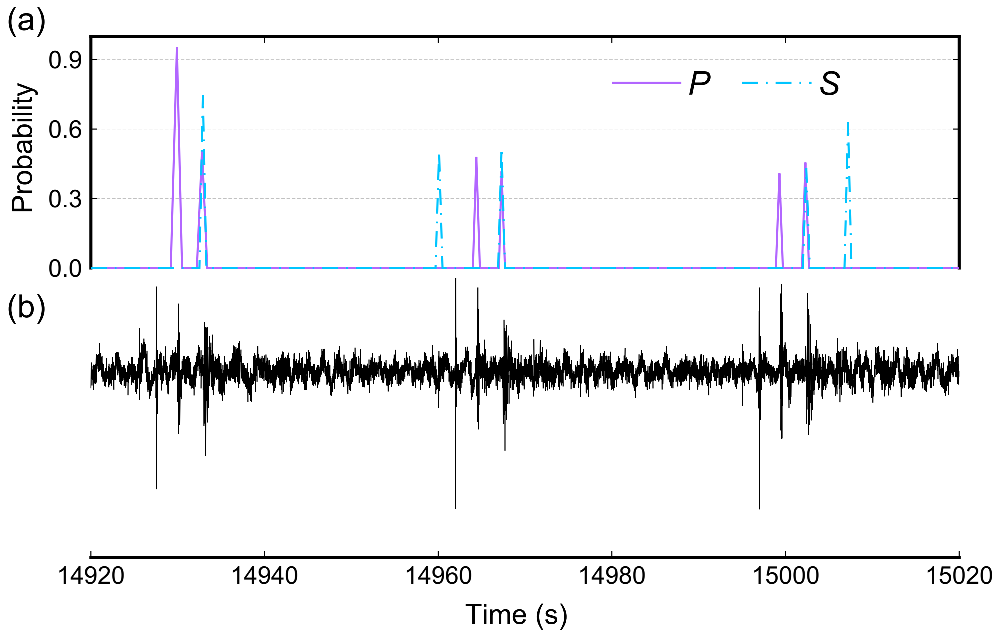

Figure 4. False positives predicted by PhaseNet. (a) The probability of *P* and *S* picks. (b) The impulsive waveforms generated by air gun sources. The color version of this figure is available only in the electronic edition.

with the maximum number of seismic picks or the grid with the smallest travel-time residual if multiple grids have the same number of picks. A total of 240 events were associated and preliminarily located in this step, after visually inspection and discarding false detection events. To estimate the apparent V_P and V_S, we fitted the distribution of the *P*- and *S*-wave travel times versus hypocentral distances after the association. The results indicate an apparent V_P of 6.41 km/s and V_S of 3.44 km/s, leading to the best-fitted V_P/V_S ratio of 1.86 (Fig. 6).

We then located the associated events with at least one *P* pick and one *S* pick and five total picks with the HYPOINVERSE algorithm (Klein, 2002) using a 1D velocity model derived from a regional 2D *P*-velocity model (Zhao *et al.*, 2018). We obtained the locations of 205 events using the HYPOINVERSE algorithm. We then used the double-difference method (Waldhauser and Ellsworth, 2000) to relocate the events. We measured the differential travel time using both existing *P* and *S* picks and waveform cross correlation. A total of 3609 *P* phase and 2654 *S* phase differential times were measured from existing picks, but only 134 *P* phase and 170 *S* phase differential times were calculated from waveform cross correlation. The number of cross-correlation differential times is quite limited because of the low waveform similarity due to the poor quality of the OBS data. During the hypoDD relocation, a minimum of five differential travel times was required to relocate each event pair within a maximum distance range of 400 km. We relocated 27 events using hypoDD, with the other 178 events remaining in their HYPOINVERSE locations.

The final catalog contains 205 events, which were all visually inspected by plotting their waveforms aligned with epicentral distance. Example waveforms of two relocated earthquakes are shown in Figure 7. Generally, the relocated events were spread across the trench, which is ~10 times more than the catalog of the USGS. Within the SCS basin, several earthquakes occurred during the period, including the one near the intersection of the Zhongnan fault zone and the extinct fossil ridge (event 1 in Figs. 7, 8a), indicating intraplate deformation does occur within the SCS basin. Importantly, abundant outer-rise earthquakes occurred both in the north and south of the Huangyan (Scarborough) Seamount chain. Clusters of shallow seismicity were observed in the outer-rise region at the south of the Huangyan (Scarborough) Seamount chain (near BB′ in Fig. 8), with focal depths of most earthquakes shallower than 10 km. In comparison, the most of outer-rise earthquakes in the north of Huangyan (Scarborough) Seamount chain were within the upper ~30 km (near AA′ in Fig. 8).

For the subduction-related earthquakes, most of the earthquakes were shallower than 100 km, and no trace of seismicity deeper than 150 km could be observed along the northern segment of the Manila trench (north of 15° N). In contrast, the area along the southern segment is characterized by relatively deep seismicity, with a maximum depth of 180 km

TABLE 1
Estimated Precision of EQTransformer and PhaseNet on Each Ocean-Bottom Seismometer (OBS) Station

Station	HY02	HY08	HY10	HY15	HY16	HY17	HY18
EQTransformer	0.65	0.81	0.74	0.72	0.83	0.81	0.85
PhaseNet	0.41	0.50	0.45	0.43	0.49	0.54	0.54

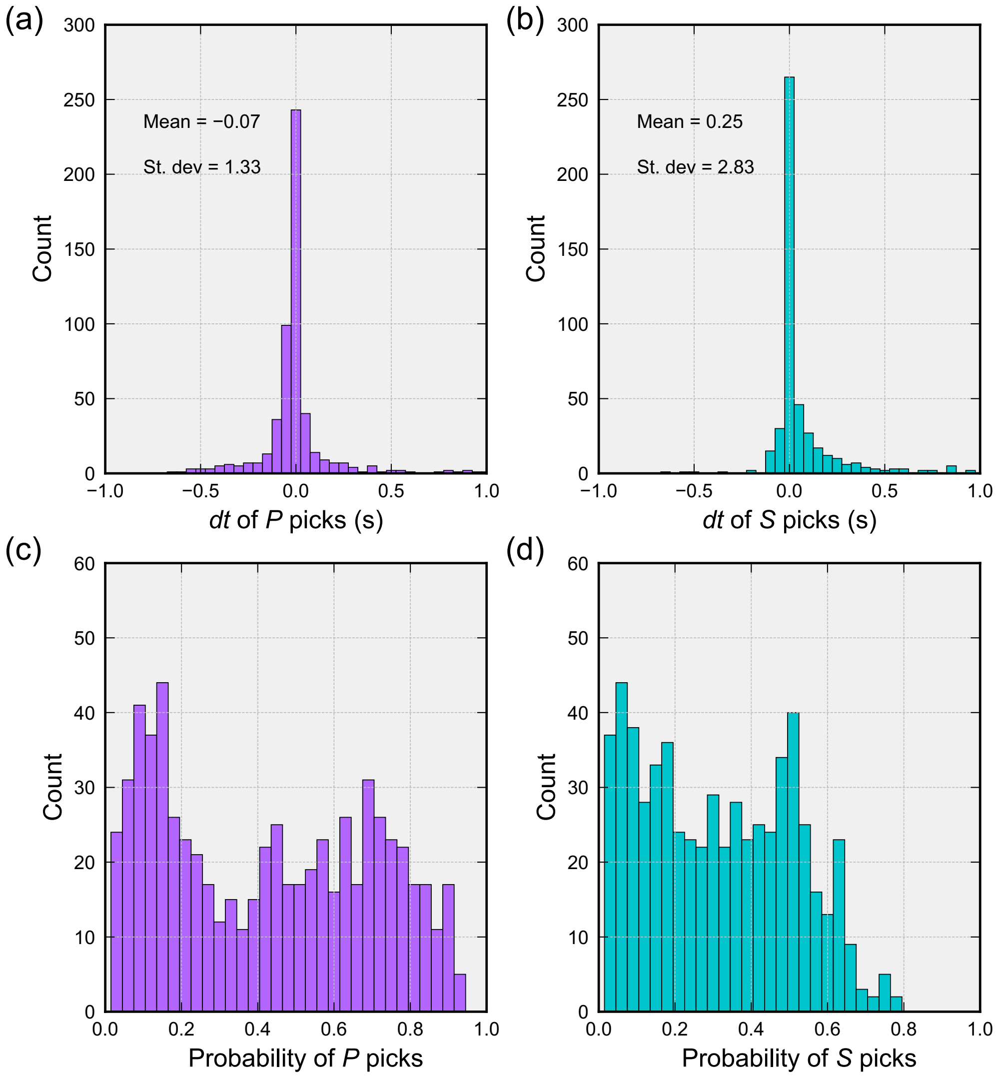

Figure 5. Differences between the arrival times of seismic phases picked by the machine learning algorithm EQTransformer and manual picks and the probability distributions of picked seismic phases. Distribution of differences in manual picks to the EQTransformer picks of (a) *P* phases and (b) *S* phases. The difference is positive when the arrival time of the seismic phase picked by the EQTransformer is later than the manually picked arrival time; otherwise, the difference is negative. Probability distribution of the seismic phases of (c) *P* waves and (d) *S* waves picked by machine learning. The color version of this figure is available only in the electronic edition.

near ~14° N (Fig. 8). The dip angles of the slab steepen southward from ~30° (Fig. 8c) to 48° (Fig. 8e) to 57° (Fig. 8e). In addition, a noticeable gap in seismicity that trends in a northeasterly direction is observed, which extends from a deeper part of the slab up to the surface at the trench line at 14–14.5° N.

Discussion

Performance of ML algorithms on OBS dataset

ML algorithms significantly improve the performance of automated tasks in seismology, which have been widely used in land-based seismic stations and have shown remarkable accuracy and processing speed for seismic signals (Perol *et al.*, 2018; Ross *et al.*, 2018). However, the application of PhaseNet and EQTransformer on OBS is quite limited. One recent study shows that their precision and recall rate are relatively lower using the OBS data in southern Mariana (Chen *et al.*, 2022). The SNR of OBS data is always low because of a variety of factors, such as poor coupling conditions, tilt noise caused by seafloor currents, compliance noise produced by pressure variations induced by ocean gravity waves, and other uncorrelated noises (Webb, 1998; Crawford and Webb, 2000).

The precision of the PhaseNet and EQTransformer automatic pickers may not be satisfactory when applied to OBS data, although both of them exhibit excellent performance on land stations. The precision, recall, and F1 score of the PhaseNet and EQTransformer are 0.96, 0.96, 0.96 and 0.99, 0.99, 0.99, respectively (Zhu and Beroza, 2019; Mousavi *et al.*, 2020). However, the precision of EQTransformer ranges from 0.65 to 0.85 on OBS stations, and the precision of PhaseNet is even lower, ranging from 0.41 to 0.54. In particular, the PhaseNet model falsely detects the impulsive signals generated by air gun sources. If including the mass of false picks of air gun signals, the precision of PhaseNet will be further reduced.

Potential bias of estimated precision is possible in this study because the number of picks used for estimating the precision is quite limited. The low precision mainly results from the generally low SNR or unusual OBS signals because of various factors. For example, tilting caused by seafloor currents affects amplitudes of three components, which may lead to pseudomorphic radiation patterns different from normal earthquakes. Some unexpected problems of polarity or horizontal orientations may also disturb OBS seismograms (Zhu *et al.*, 2020). Besides, this can be attributed to the fact that no OBS data were used in the training, so the false detection rate was high when

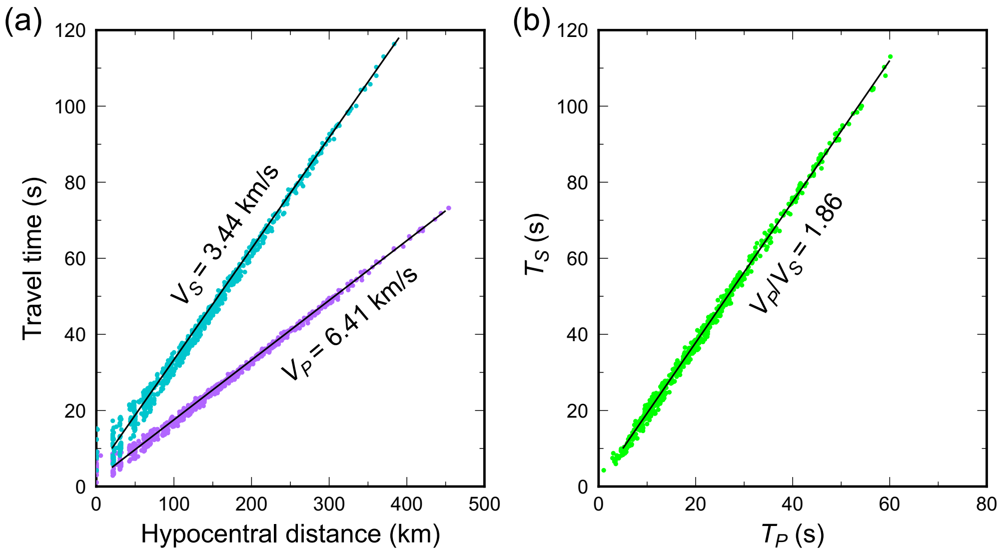

Figure 6. Distribution of the travel times of seismic phases associated by the Rapid Earthquake Association and Location package (REAL) method and the fitting of V_P/V_S. (a) Travel times of seismic phases associated and located using the REAL method. The purple (cyan) dots signify the relationship between the travel time of the seismic phase of the *P* wave (*S* wave) and the hypocentral distance. The slopes of black lines indicate the best-fitted V_P (6.41 km/s) and V_S (3.44 km/s). (b) Fitted VP/V_S ratio of 1.86 based on the travel times. The color version of this figure is available only in the electronic edition.

processing OBS data. Because of limited OBS data and labeled seismic signals from OBS recordings, a well-trained ML model suitable for OBS data is lacking by far. The catalog for the region could be further trained for an improved ML model for active subduction zones.

Implications for the regional tectonic features

The seismicity can illuminate the presence of active faults and can serve as proxies that denote changes in slab geometry and potential slab tears, although this might not be representative of long-term seismic activity in this region.

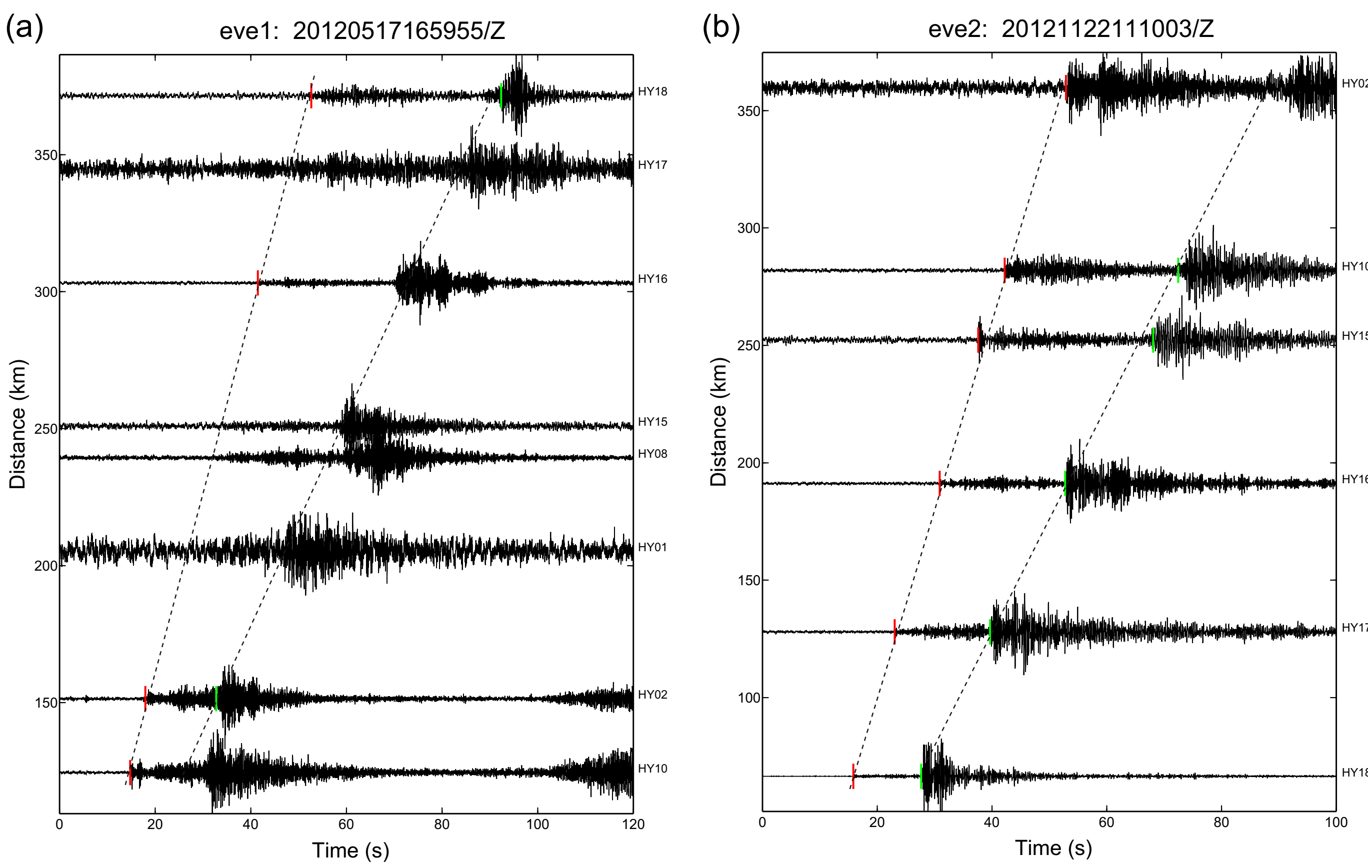

Figure 7. Waveforms of two relocated events: (a) event 1 near Zhongnan Fault zone and (b) event 2 at east of the trench, for which locations are marked as stars in Figure 8a. The red and green bars represent *P* and *S* picks by EQTransformer. The color version of this figure is available only in the electronic edition.

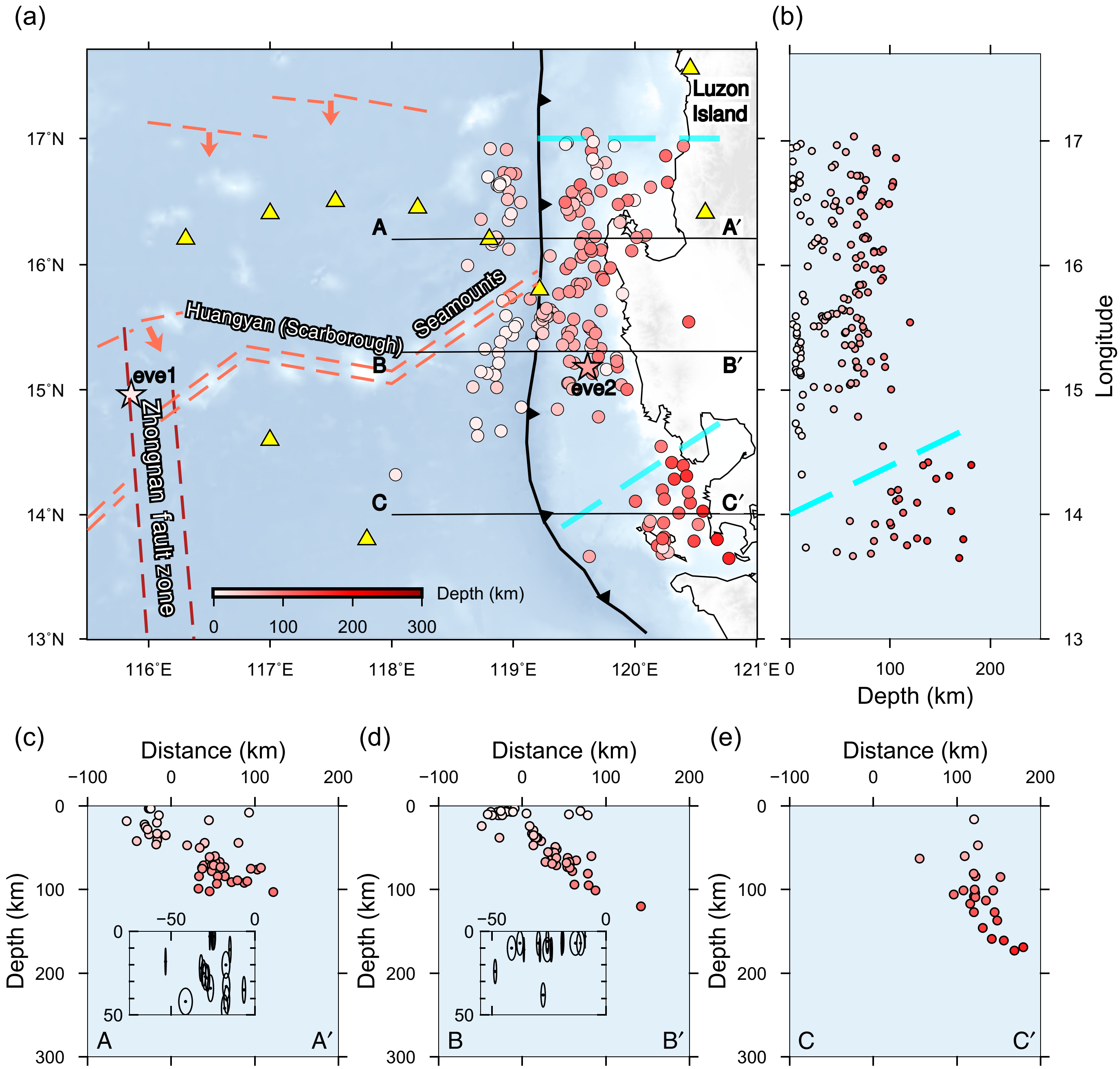

Figure 8. The distribution of relocated earthquakes from our final catalog. (a) Map view of the relocated events. The dots represent located earthquakes colored by depth. The three black lines mark the location of cross sections. The other captions are same as Figure 1. (b) The depth distribution of earthquakes along the longitude direction. The cyan dashed line marks the position of a potential slab tear. (c–e) Cross-section views of the relocated events from our final catalog. The inset panels zoom in the cross sections of outer-rise earthquakes with the error ellipses indicating the location uncertainties given by HYPOINVERSE algorithm. The color version of this figure is available only in the electronic edition.

Outer-rise seismicity. The outer-rise seismicity provides a useful constraint on the plate bending. Abundant earthquakes have been found in the outer-rise region in various subduction zones (e.g., Zhu *et al.*, 2019; Chen *et al.*, 2022; Guo *et al.*, 2022). A notable difference is the existence of bending fault earthquakes at the northern of Huangyan (Scarborough) Seamount chain, where is lacking seismicity in the historical USGS and Global Centroid Moment Tensor recordings. The outer-rise seismicity in the northern of Huangyan (Scarborough) Seamount chain is deeper than the south. The variation in outer-rise seismicity may be the proxy of active bending faulting, indicating intertrench changes in bending stresses (Zhou *et al.*, 2015; Zhang, Sun, *et al.*, 2018). Compared with other subduction zones, the depths of most outer-rise earthquakes in Manila are shallower than that near the Mariana trench (>40 km) (Chen *et al.*, 2022) and offshore southern Taiwan (44–50 km) (Tan, 2020). The results are consistent with the numerical models that the plate age can be a dominant factor in controlling the bending shape for relatively young subducting plates, for example, the Manila (16–36 Ma) and the old subducting plates, for example, the Mariana (140–160 Ma) (Zhang, Lin, *et al.*, 2018).

The bending faults may serve as pathways for seawater to enter the slab's interior, facilitating the formation of hydration minerals and leading to a pervasively serpentinized region (Shillington *et al.*, 2015; Fujie *et al.*, 2016; Zhu *et al.*, 2021). The region has a slightly higher apparent V_P/V_S of 1.86 than the average regular oceanic crust composition (Christensen, 2004), which may indicate the presence of serpentine. Anomalously high V_P/V_S ratio close to 2.0 is also observed at the south of the ridge using receiver functions (Hung *et al.*, 2021). Serpentinites have also been widely observed at slow and ultraslow spreading ridges where offset normal faults and detachment faults commonly form (Sauter *et al.*, 2013; Guillot *et al.*, 2015). The bending faults near the trench and faults related to the extinct fossil ridges may both contribute to forming hydrated minerals.

Slab tear. The Wadati–Benioff zone seismicity is ambiguous near the extinct MOR based on the historical catalog (Fig. 2c), partly because of the lack of near-field observational data, also ascribed to the complexity of the tectonic environment of the region. By analyzing historical seismic catalogs in the region, the segmentation of Wadati–Benioff zone seismicity has been hypothesized to be related to the subduction of the extinct MOR at 16–17° N, in which a slab window is proposed along the Manila trench (Bautista *et al.*, 2001). The seismological tomographic results also show along-strike variational slab images, suggesting a slab tear along the ridge beneath Luzon Island (Fan *et al.*, 2014).

The results clearly trace the Waditi–Beniof zone seismicity near the extinct MOR, which improves constraints on the subducted slab. Combined with historical seismicity, the observed change in dip from shallow to steep southward along the trench may indicate a slab tear at the south of ~18° N, which is spatially correlated with the subduction of the extinct MOR. Slab tearing may affect mantle processes and the long-term geodynamic evolution of continents, which may be responsible for the abrupt termination of the eastern chain of volcanoes south of 18° N on Luzon Island (Yang *et al.*, 1996). The subducted ridge may serve as the weakest zone where slab tear could be localized (Bautista *et al.*, 2001). Subducted oceanic ridges inducing slab tears are also observed in the Nazca slab beneath the South American subduction zone, which is characterized by lateral variations in slab dip angle (Scire *et al.*, 2015; Lynner *et al.*, 2017).

In addition to the potential slab tear related to the extinct MOR near 17° N, it is also likely a slab tear between 14 and 14.5° N, in which a seismic gap trending in a northeasterly direction. From this point southward, the segment of the Manila trench bends sharply to the east-southeast. Besides, the seismicity of the southern segment is distinctly deeper than the segment north of 15° N. The earthquakes are down to a depth of ~180 km in this study, and deep historical seismicity extends up to a depth of ~240 km. A slab tear can occur because of along-strike changes in slab geometry, which may be associated with the sharp bending of the slab caused by the collision of a microcontinental plate with the islands (Bautista *et al.*, 2001). The slab tear may result in the seismic gap between 14 and 14.5° N.

The variation in slab geometry and the subducted seamounts may affect the megathrust earthquake rupture and earthquake potential along the Manila trench. The geometrical segmentation of the slab can host ruptures on either segments but likely inhibits rupture of the entire fault to generate earthquakes with magnitudes greater than M_w 8.5. (Yu *et al.*, 2018). Indeed, it has been suggested that fault geometry can be the first-order factor controlling earthquake rupture behaviors by increasing shear strength heterogeneity (e.g., King, 1986; Bletery *et al.*, 2016), in addition to heteorogeneous stress and frictional properties (e.g., Yang *et al.*, 2019, 2022; Yao and Yang, 2022). In addition, the Huangyan (Scarborough) Seamount chain could act as a barrier in stopping megathrust ruptures. Previous studies have discussed the barrier effects of subducted seamounts on coseismic ruptures (e.g., Yang *et al.*, 2012, 2013). Subducted seamounts could stop coseismic ruptures by various mechanisms, such as increasing frictional resistance (Kodaira *et al.*, 2000), increasing normal stress on the thrust interface (Scholz and Small, 1997), or reducing elastic strain accumulation due to low effective normal stress of fluid-rich sediments near seamounts (Mochizuki *et al.*, 2008).

Summary

We apply the ML-based algorithms, EQTransformer and PhaseNet, to the OBS dataset in the SCS for detecting seismic events and picking phases. We evaluate the precision of the two algorithms and analyze the picking uncertainties by comparing the time residuals. The PhaseNet has low precision compared with EQTransformer on OBS data and is significantly disturbed by impulsive air gun signals.

Based on the detected seismic phases by EQTransformer, we relocate the detected events and derive a catalog of earthquakes for the duration of the temporary OBS deployment. The final catalog contains 205 located earthquakes in the region, which is ~10 times the USGS catalog. Most of the relocated earthquakes are near the Manila trench, but a few occur within the SCS basin. In the outer-rise region, tens of bending-fault earthquakes occur at the northern of the Huangyan (Scarborough) Seamount chain, where there is no seismicity in the historical recordings. The variation in outer-rise seismicity may be the proxy of active bending faulting, indicating intertrench changes in bending stresses. For slab-related earthquakes, most of them are shallower than 100 km north of 15° N. The focal depths of slab-related earthquakes gradually deepen to ~200 km southward along the trench, indicating slab tears related to the extinct MOR or sharp bending of the slab.

Data and Resources

The ocean-bottom seismometer data for earthquakes used in this study can access by connecting with the corresponding authors. We collected seismograms of the two Global Seismographic Network stations via the Incorporated Research Institutions for Seismology. The historical earthquake catalog was searched using https://earthquake.usgs.gov/earthquakes/search. The Global Centroid Moment Tensor Project database was searched using www.globalcmt.org/CMTsearch.html. All websites were last accessed in July 2022.

Declaration of Competing Interests

The authors acknowledge that there are no conflicts of interest recorded.

Acknowledgments

This work is supported by National Natural Science Foundation of China (Grant Numbers 92158205, 92058209, and 91958211), an award from the Center for Ocean Research in Hong Kong and Macau (a joint research center for ocean research between Qingdao Pilot National Laboratory for Marine Science and Technology and The Hong Kong University of Science and Technology), Hong Kong Research Grant Council grants (Grant Number 14304820), Gaohua Zhu's stand-up fund, Shenzhen Science and Technology Program (Grant Numbers KQTD20170810111725321 and JCYJ20180504170422082), and a Youth Innovation Promotion Association Chinese Academy of Sciences Grant (Grant Number 2016189). The authors thank Qingsheng Guan from the Second Institute of Oceanography, Ministry of Natural Resources, for sharing the updated position of extinct fossil ridges. The authors thank the two reviewers and editor for insightful suggestions.

References

Bautista, B. C., M. L. P. Bautista, K. Oike, F. T. Wu, and R. S. Punongbayan (2001). A new insight on the geometry of subducting slabs in northern Luzon, Philippines, *Tectonophysics* **339,** nos. 3/4, 279–310, doi: 10.1016/S0040-1951(01)00120-2.

Bletery, Q., A. M. Thomas, A. W. Rempel, L. Karlstrom, A. Sladen, and L. De Barros (2016). Mega-earthquakes rupture flat megathrusts, *Science* **354,** no. 6315, 1027–1031, doi: 10.1126/science.aag0482.

Briais, A., P. Patriat, and P. Tapponnier (1993). Updated interpretation of magnetic anomalies and seafloor spreading stages in the south China Sea: Implications for the Tertiary tectonics of Southeast Asia, *J. Geophys. Res.* **98,** no. B4, 6299–6328, doi: 10.1029/92jb02280.

Chang, J.-H., H.-S. Yu, T.-Y. Lee, H.-H. Hsu, C.-S. Liu, and Y.-T. Tsai (2013). Characteristics of the outer rise seaward of the Manila Trench and implications in Taiwan–Luzon convergent belt, South China Sea, *Mar. Geophys. Res.* **33,** no. 4, 351–367, doi: 10.1007/s11001-013-9168-6.

Chen, H., H. Yang, G. Zhu, M. Xu, J. Lin, and Q. You (2022). Deep outer-rise faults in the southern mariana subduction zone indicated by a machine-learning-based high-resolution earthquake catalog, *Geophys. Res. Lett.* **49,** no. 12, doi: 10.1029/2022gl097779.

Christensen, N. I. (2004). Serpentinites, peridotites, and seismology, *Int. Geol. Rev.* **46,** no. 9, 795–816, doi: 10.2747/0020-6814.46.9.795.

Craig, T. J., A. Copley, and J. Jackson (2014). A reassessment of outer-rise seismicity and its implications for the mechanics of oceanic lithosphere, *Geophys. J. Int.* **197,** no. 1, 63–89, doi: 10.1093/gji/ggu013.

Crawford, W. C., and S. C. Webb (2000). Identifying and removing tilt noise from low-frequency (>0.1 Hz) seafloor vertical seismic data, *Bull. Seismol. Soc. Am.* **90,** no. 4, 952–963, doi: 10.1785/0119990121.

Eimer, M., D. A. Wiens, C. Cai, D. Lizarralde, and H. Jasperson (2020). Seismicity of the incoming plate and forearc near the mariana trench recorded by ocean bottom seismographs, *Geochem. Geophys. Geosys.* **21,** no. 4, doi: 10.1029/2020gc008953.

Fan, J., S.-G. Wu, and G. Spence (2014). Tomographic evidence for a slab tear induced by fossil ridge subduction at Manila Trench, South China Sea, *Int. Geol. Rev.* **57,** nos. 5/8, 998–1013, doi: 10.1080/00206814.2014.929054.

Fujie, G., S. Kodaira, T. Sato, and T. Takahashi (2016). Along-trench variations in the seismic structure of the incoming Pacific plate at the outer rise of the northern Japan Trench, *Geophys. Res. Lett.* **43,** no. 2, 666–673, doi: 10.1002/2015gl067363.

Gong, J., W. Fan, and R. Parnell-Turner (2022). Microseismicity indicates atypical small-scale plate rotation at the Quebrada transform fault system, east pacific rise, *Geophys. Res. Lett.* **49,** no. 3, doi: 10.1029/2021gl097000.

Guan, Q., T. Zhang, B. Taylor, J. Gao, and J. Li (2021). Ridge jump reorientation of the South China Sea revealed by high-resolution magnetic data, *Terra Nova* **33,** no. 5, 475–482, doi: 10.1111/ter.12532.

Guillot, S., S. Schwartz, B. Reynard, P. Agard, and C. Prigent (2015). Tectonic significance of serpentinites, *Tectonophysics* **646,** 1–19, doi: 10.1016/j.tecto.2015.01.020.

Guo, L., J. Lin, H. Yang, and J. Tian (2022). Aftershocks of the 2012 Mw 8.6 Wharton Basin intraplate earthquake in the eastern Indian Ocean revealed by near-field ocean-bottom seismometers, *Seismol. Res. Lett.* doi: 10.1785/0220210096.

He, L., K. Wang, L. Xiong, and J. Wang (2001). Heat flow and thermal history of the South China Sea, *Phys. Earth Planet. In.* **126,** nos. 3/4, 211–220, doi: 10.1016/s0031-9201(01)00256-4.

Hung, T. D., B. M. Le, Y. Yu, M. Xue, B. Liu, C. Liu, J. Wang, M. Pan, P.T. Huong, and F. Liu (2021). Crustal structure across the extinct mid-ocean ridge in South China sea from OBS receiver functions: Insights into the spreading rate and magma supply prior to the Ridge cessation, *Geophys. Res. Lett.* **48,** no. 3, doi: 10.1029/2020gl089755.

Jiang, C., P. Zhang, M. C. A. White, R. Pickle, and M. S. Miller (2022). A detailed earthquake catalog for banda arc–Australian plate collision zone using machine-learning phase picker and an automated workflow, *Seism. Rec.* **2,** no. 1, 1–10, doi: 10.1785/0320210041.

King, G. C. P. (1986). Speculations on the geometry of the initiation and termination process of earthquake rupture and its relation to morphology and geological structure, *Pure Appl. Geophys.* **124,** no. 3, 567–585.

Klein, F. W. (2002). User's guide to HYPOINVERSE-2000, a Fortran program to solve for earthquake locations and magnitudes, *Report Rept. 2002-171*, 123 pp.

Kodaira, S., N. Takahashi, A. Nakanishi, S. Miura, and Y. Kaneda (2000). Subducted seamount imaged in the rupture zone of the 1946 Nankaido earthquake, *Science* **289,** 104–106.

Lay, T., C. J. Ammon, H. Kanamori, M. J. Kim, and L. Xue (2011). Outer trench-slope faulting and the 2011 Mw 9.0 off the Pacific coast of Tohoku earthquake, *Earth Planets Space* **63,** no. 7, 713–718, doi: 10.5047/eps.2011.05.006.

Lay, T., C. J. Ammon, H. Kanamori, L. Rivera, K. D. Koper, and A. R. Hutko (2010). The 2009 Samoa-Tonga great earthquake triggered doublet, *Nature* **466,** no. 7309, 964–968, doi: 10.1038/nature09214.

Le, B. M., T. Yang, Y. J. Chen, and H. Yao (2018). Correction of OBS clock errors using Scholte waves retrieved from cross-correlating hydrophone recordings, *Geophys. J. Int.* **212,** no. 2, 891–899.

Li, C.-F., X. Xu, J. Lin, Z. Sun, J. Zhu, Y. Yao, X. Zhao, Q. Liu, D. K. Kulhanek, J. Wang, and T. Song (2014). Ages and magnetic structures of the South China Sea constrained by deep tow magnetic surveys and IODP Expedition 349, *Geochem. Geophys. Geosys.* **15,** no. 12, 4958–4983, doi: 10.1002/2014gc005567.

Li, C.-F., Z. Zhou, J. Li, B. Chen, and J. Geng (2008). Magnetic zoning and seismic structure of the South China Sea ocean basin, *Mar. Geophys. Res.* **29,** no. 4, 223–238, doi: 10.1007/s11001-008-9059-4.

Li, L., Q. Qiu, Z. Li, and P. Zha ng (2022). Tsunami hazard assessment in the South China Sea: A review of recent progress and research gaps, *Sci. China Earth Sci.* **65,** no. 5, 783–809, doi: 10.1007/s11430-021-9893-8.

Liu, C., Q. Hua, Y. Pei, T. Yang, S. Xia, M. Xue, B. M. Le, D. Huo, F. Liu, and H. Huang (2014). Passive-source ocean bottom seismograph (OBS) array experiment in South China Sea and data quality analyses, *Chin. Sci. Bull.* **59,** no. 33, 4524–4535, doi: 10.1007/s11434-014-0369-4.

Liu, Y., B. Liu, C. Liu, and Q. Hua (2020). The crustal structure of the Eastern Subbasin of the South China Sea: Constraints from receiver functions, *Geophys. J. Int.* **222,** no. 2, 1003–1012, doi: 10.1093/gji/ggaa246.

Lynner, C., M. L. Anderson, D. E. Portner, S. L. Beck, and H. Gilbert (2017). Mantle flow through a tear in the Nazca slab inferred from shear wave splitting, *Geophys. Res. Lett.* **44,** no. 13, 6735–6742, doi: 10.1002/2017gl074312.

Masson, D. G. (1991). Fault patterns at outer trench walls, *Mar. Geophys. Res.* **13,** no. 3, 209–225, doi: 10.1007/bf00369150.

Mochizuki, K., T. Yamada, M. Shinohara, Y. Yamanaka, and T. Kanazawa (2008). Weak inter-plate coupling by seamounts and repeating M∼7 earthquakes, *Science* **321,** 1194–1197.

Mousavi, S. M., W. L. Ellsworth, W. Zhu, L. Y. Chuang, and G. C. Beroza (2020). Earthquake transformer-an attentive deep-learning model for simultaneous earthquake detection and phase picking, *Nat. Commun.* **11,** no. 1, 3952, doi: 10.1038/s41467-020-17591-w.

Park, Y., S. M. Mousavi, W. Zhu, W. L. Ellsworth, and G. C. Beroza (2020). Machine-learning-based analysis of the Guy-Greenbrier, Arkansas earthquakes: A tale of two sequences, *Geophys. Res. Lett.* **47,** no. 6, doi: 10.1029/2020gl087032.

Perol, T., M. Gharbi, and M. Denolle (2018). Convolutional neural network for earthquake detection and location, *Sci. Adv.* **4,** no. 2, e1700578, doi: 10.1126/sciadv.1700578.

Ross, Z. E., M. A. Meier, and E. Hauksson (2018). P wave arrival picking and first-motion polarity determination with deep learning, *J. Geophys. Res.* **123,** no. 6, 5120–5129, doi: 10.1029/2017jb015251.

Sauter, D., M. Cannat, S. Rouméjon, M. Andreani, D. Birot, A. Bronner, D. Brunelli, J. Carlut, A. Delacour, V. Guyader, *et al.* (2013). Continuous exhumation of mantle-derived rocks at the Southwest Indian Ridge for 11 million years, *Nature Geosci.* **6,** no. 4, 314–320, doi: 10.1038/ngeo1771.

Scholz, C. H., and C. Small (1997). The effect of seamount subduction on seismic coupling, *Geology* **25,** 487–490.

Scire, A., G. Zandt, S. Beck, M. Long, L. Wagner, E. Minaya, and H. Tavera (2015). Imaging the transition from flat to normal subduction: Variations in the structure of the Nazca slab and upper mantle under southern Peru and northwestern Bolivia, *Geophys. J. Int.* **204,** no. 1, 457–479, doi: 10.1093/gji/ggv452.

Shillington, D. J., A. Bécel, M. R. Nedimović, H. Kuehn, S. C. Webb, G. A. Abers, K. M. Keranen, J. Li, M. Delescluse, and G. A. Mattei-Salicrup (2015). Link between plate fabric, hydration and subduction zone seismicity in Alaska, *Nature Geosci.* **8,** 961, doi: 10.1038/ngeo2586.

Tan, E. (2020). Subduction of transitional crust at the Manila Trench and its geophysical implications, *J. Asian Earth Sci.* **187,** doi: 10.1016/j.jseaes.2019.104100.

Tan, Y. J., F. Waldhauser, W. L. Ellsworth, M. Zhang, W. Zhu, M. Michele, L. Chiaraluce, G. C. Beroza, and M. Segou (2021). Machine-learning-based high-resolution earthquake catalog reveals how complex fault structures were activated during the 2016–2017 Central Italy sequence, *Seism. Rec.* **1,** no. 1, 11–19, doi: 10.1785/0320210001.

Waldhauser, F., and W. L. Ellsworth (2000). A double-difference earthquake location algorithm: Method and application to the northern Hayward Fault, California, *Bull. Seismol. Soc. Am.* **90,** no. 6, 1353–1368, doi: 10.1785/0120000006.

Webb, S. C. (1998). Broadband seismology and noise under the ocean, *Rev. Geophys.* **36,** no. 1, 105–142, doi: 10.1029/97rg02287.

Wong, W. C. J., J. P. Zi, H. F. Yang, and J. R. Su (2021). Spatial-temporal evolution of injection induced earthquakes in weiyuan area by machinelearning phase picker and waveform cross-correlation, *Earth Planet. Phys.* **5,** no. 6, 485–500, doi: 10.26464/epp2021055.

Yang, H., Y. Liu, and J. Lin (2012). Effects of subducted seamounts on megathrust earthquake nucleation and rupture propagation, *Geophys. Res. Lett.* **39,** no. 24, L24302, doi: 10.1029/2012GL053892.

Yang, H., Y. Liu, and J. Lin (2013). Geometrical effects of a subducted seamount on stopping megathrust ruptures, *Geophys. Res. Lett.* **40,** no. 10, 2011–2016, doi: 10.1002/grl.50509.

Yang, H., S. Yao, and X. Chen (2022). Rupture propagation on heterogeneous fault: Challenges for predicting earthquake magnitude, *Chin. Sci. Bull.* **67,** 1–14, doi: 10.1360/TB-2021-1086.

Yang, H., S. Yao, B. He, and A. Newman (2019). Earthquake rupture dependence on hypocentral location along the Nicoya Peninsula subduction megathrust, *Earth Planet. Sci. Lett.* **520,** 10–17, doi: 10.1016/j.epsl.2019.05.030.

Yang, T. F., T. Lee, C.-H. Chen, S.-N. Cheng, U. Knittel, R. S. Punongbayan, and A. R. Rasdas (1996). A double island arc between Taiwan and Luzon: Consequence of ridge subduction, *Tectonophysics* **258,** nos. 1/4, 85–101, doi: 10.1016/0040-1951(95)00180-8.

Yao, S., and H. Yang (2022). Hypocentral dependent shallow slip distribution and rupture extents along a strike-slip fault, *Earth Plant. Sci. Lett.* **578,** doi: 10.1016/j.epsl.2021.117296.

Yu, H., Y. Liu, H. Yang, and J. Ning (2018). Modeling earthquake sequences along the Manila subduction zone: Effects of three-dimensional fault geometry, *Tectonophysics* **733,** 73–84, doi: 10.1016/j.tecto.2018.01.025.

Zhang, F., J. Lin, Z. Zhou, H. Yang, and W. Zhan (2018). Intra- and intertrench variations in flexural bending of the Manila, Mariana and global trenches: Implications on plate weakening in controlling trench dynamics, *Geophys. J. Int.* **212,** no. 2, 1429–1449, doi: 10.1093/gji/ggx488.

Zhang, J., Z. Sun, M. Xu, H. Yang, Y. Zhang, and F. Li (2018). Lithospheric 3-D flexural modelling of subducted oceanic plate with variable effective elastic thickness along the Manila Trench, *Geophys. J. Int.* **215,** no. 3, 2071–2092, doi: 10.1093/gji/ggy393.

Zhang, J., F. Zhang, H. Yang, J. Lin, and Z. Sun (2022). The effects of plateau subduction on plate bending, stress and intraplate seismicity, *Terra Nova* **34,** 113–122, doi: 10.1111/ter.12570.

Zhang, M., W. L. Ellsworth, and G. C. Beroza (2019). Rapid earthquake association and location, *Seismol. Res. Lett.* **90,** no. 6, 2276–2284, doi: 10.1785/0220190052.

Zhao, M., E. He, J.-C. Sibuet, L. Sun, X. Qiu, P. Tan, and J. Wang (2018). Postseafloor spreading volcanism in the central east south china sea and its formation through an extremely thin oceanic crust, *Geochem. Geophys. Geosys.* **19,** no. 3, 621–641, doi: 10.1002/2017gc007034.

Zhou, P., W. L. Ellsworth, H. Yang, Y. Joe Tan, G. C. Beroza, M. Sheng, and R. Chu (2021). Machine-learning-facilitated earthquake and anthropogenic source detections near the Weiyuan Shale Gas Blocks, Sichuan, China, *Earth Planet. Phys.* **5,** no. 6, 501–519, doi: 10.26464/epp2021053.

Zhou, Z., J. Lin, M. D. Behn, and J. A. Olive (2015). Mechanism for normal faulting in the subducting plate at the Mariana Trench, *Geophys. Res. Lett.* **42,** no. 11, 4309–4317, doi: 10.1002/2015GL063917.

Zhu, G., J. Lin, H. Yang, and Q. You (2020). Determining the orientation of ocean-bottom seismometers on the seafloor and correcting for polarity flipping via polarization analysis and waveform modeling, *Seismol. Res. Lett.* **91,** no. 2A, 814–825, doi: 10.1785/0220190239.

Zhu, G., D. A. Wiens, H. Yang, J. Lin, M. Xu, and Q. You (2021). Upper Mantle hydration indicated by decreased shear velocity near the southern mariana trench from Rayleigh wave tomography, *Geophys. Res. Lett.* **48,** no. 15, doi: 10.1029/2021gl093309.

Zhu, G., H. Yang, J. Lin, Z. Zhou, M. Xu, J. Sun, and K. Wan (2019). Along-strike variation in slab geometry at the southern Mariana subduction zone revealed by seismicity through ocean bottom seismic experiments, *Geophys. J. Int.* **218,** no. 3, 2122–2135, doi: 10.1093/gji/ggz272.

Zhu, G., H. Yang, Y. J. Tan, M. Jin, X. Li, and W. Yang (2022). The cascading foreshock sequence of the Ms 6.4 Yangbi earthquake in Yunnan, China, *Earth Planet. Sci. Lett.* **591,** doi: 10.1016/j.epsl.2022.117594.

Zhu, W., and G. C. Beroza (2019). PhaseNet: A deep-neural-network-based seismic arrival time picking method, *Geophys. J. Int.* doi: 10.1093/gji/ggy423.

Manuscript received 21 September 2022
Published online 2 December 2022